ORIGINAL PAPER

Modeling rapidly growing cracks in planar materials with a view to micro structural effects

J. Persson · P. Isaksson

Abstract Dynamic fracture behavior in both fairly continuous materials and discontinuous cellular materials is analyzed using a hybrid particle model. It is illustrated that the model remarkably well captures the fracture behavior observed in experiments on fast growing cracks reported elsewhere. The material's microstructure is described through the configuration and connectivity of the particles and the model's sensitivity to a perturbation of the particle configuration is judged. In models describing a fairly homogeneous continuous material, the microstructure is represented by particles ordered in rectangular grids, while for models describing a discontinuous cellular material, the microstructure is represented by particles ordered in honeycomb grids having open cells. It is demonstrated that small random perturbations of the grid representing the microstructure results in scatter in the crack growth velocity. In materials with a continuous microstructure, the scatter in the global crack growth velocity is observable, but limited, and may explain the small scattering phenomenon observed in experiments on high-speed cracks in e.g. metals. A random perturbation of the initially ordered rectangular grid does however not change the average macroscopic crack growth velocity estimated from a set of models having different grid perturbations and imply that the microstructural discretization is of limited importance when predicting the global crack behavior in fairly continuous materials. On the other hand, it is shown that a similar perturbation of honeycomb grids, representing a material with a discontinuous cellular microstructure, result in a considerably larger scatter effect and there is also a clear shift towards higher crack growth velocities as the perturbation of the initially ordered grid become larger. Thus, capturing the discontinuous microstructure well is important when analyzing growing cracks in cellular or porous materials such as solid foams or wood.

J. Persson (✉)
Department of Engineering Physics, Mid Sweden University, 85170 Sundsvall, Sweden
e-mail: Johan.Persson@miun.se

P. Isaksson
Applied Mechanics, The Ångström Laboratory, Uppsala University, Box 534, 75121 Uppsala, Sweden

1 Introduction

Recently the authors proposed a three-dimensional mechanical model to capture dynamic fractures in heterogeneous materials (Persson and Isaksson 2014). The focus in the previous study was on discontinuous fiber-based materials, but the model is equally well suited for more continuous materials, as will be further revealed here. Modeling dynamic fractures has evolved from the classical static fracture criterion by Griffith (1920) via quasi-static crack growth to full dynamics (cf. Nilsson 2001; Freund 1998). Some of the different methods of modeling dynamic cracks are analytical

(Gehlen et al. 1987; Popelar and Gehlen 1987), while others are numerical, such as the finite element method (Ramulu and Kobayashi 1985), the extended finite element method (Belytschko et al. 2009) and so-called "mesh-free methods" (Mos et al. 1999). Lattice models (LM) pioneered by Hrennikoff (1941) are conceptually near to the FE models but with a different history. While FEM stems from discretizing a continuum, LMs share a history with molecular dynamics (MD) and has later been adapted to deal with effective material points rather than atoms cf. Ostoja-Starzewski et al. (1996). A third class of models is the morphology based models where the discretization is made to correspond to actual physical micro structures. In resent years particle methods have entered the scene, e.g. hybrid particle element methods (Fahrenthold and Horban 2001; Rabb and Fahrenthold 2010; Monteiro Azevedo and Lemos 2006) and peridynamics (Silling and Bobaru 2005; Silling and Askari 2005; Ha and Bobaru 2010) or discrete element methods (Persson and Isaksson 2013, 2014). The distinction between particle and hybrid particle element method is not absolute, however the hybrid methods often have the possibility to model new contacts and use interactions known from mechanics such as trusses and shells (Rabb and Fahrenthold 2010) whilst in the general case other potentials are common such as the Lenord-Jones cf. (Gao 1996), or longer reaching interactions cf. (Silling and Bobaru 2005, Wang et al. 2009). There is also a class of morphology based particle methods, such as the one used in this paper. All three classes of particle models are examples of LM. The traditional analytical solutions have limited usefulness for practical problems, but they provide a basis on which the computational (numerical) models stand and serves as benchmark problems. Finite element models are perhaps the most established methods to model stationary cracks and fractures. However, they are less suited for modeling growing cracks for mainly two reasons: (1) the material description needs to be continuous and, (2) re-meshing strategies are needed to capture the changed geometry when a crack grows. The first problem has been partly solved by the introduction of the extended finite element method, also known as the generalized finite element method, in which a crack can extend through split elements. The second problem has been met by introduction of "mesh-free" methods such as the boundary element method. However, a significant drawback of the boundary element method is the difficulty to include material non-

linearities and anisotropy, cf. Zang and Gudmundson (1988). Moreover, while analytical methods are computationally inexpensive they are of limited practical use when analyzing fracture in engineering structures of arbitrary geometry because of the complex interactions between the crack and other surfaces (e.g. boundaries). In this case, numerical models become necessary (cf. Nilsson 2001). Even though e.g. crack paths often can be fairly accurate estimated by a quasistatic method, the crack growth velocities needs to be determined by other means cf. (Ooi and Yang 2011). In the LM class any lattice-lattice interaction may be used, and for modeling linear elastic fracture a popular choice is spring network models (Ostoja-Starzewski et al. 1996). Some extensions to the simple springs are made to adjust the Poisons ratio by the introduction of torsion spring and beams cf. (Ostoja-Starzewski et al. 1996; Wang et al. 2009). Such models are commonly used to model fracture with implicit solutions cf. (Ostoja-Starzewski et al. 1996; Suiker et al. 2001; Marder and Liu 1993) or by solving embedded differential equations to compute favorable crack speeds cf. (Marder and Liu 1993). To model a growing crack with a physical dynamic behavior, it is possible to use a particle representation of the material with mechanical interaction laws and advance in time using Newton's equation of motion rather than the quasi-static motion favored in e.g. traditional finite element models. The interaction laws might be based on e.g. piecewise continuum mechanics, like the hybrid particle element method, or non-local interaction laws such in peridynamics cf. (Silling and Bobaru 2005; Silling and Askari 2005). These methods are inherently dynamic in the sense that the crack velocity is a result of the material parameters, rather than a separate material parameter to be set (cf. Persson and Isaksson 2014). If the previously mentioned models are sorted by mathematical similarities new groupings would arise, with the major groupings; non linear versus linear radial interactions, radial versus radial and angular interactions eg. spring type versus beam type interactions, in the case of angular interactions rigid versus elastic versus freely rotating connections between elements, whether or not the discretization represent a physical entity or is an arbitrary discretization. Finally there is the option whether to advance in time explicit or implicit, which refers to advancing in time using Newtonian mechanics or some quasistatic means of time dependent evolution and an explicit integration does not exclude the

possibility of an implicit integration scheme such as Rungekutta.

Lets explore the last choice first: Depending on the available computational resources, advancing in time implicitly without inertia may be the only realistic possibility and it is thus a popular choice cf. (Ostoja-Starzewski et al. 1996; Suiker et al. 2001; Marder and Liu 1993; Gerstle et al. 2007; Bolander and Saito 1998). Including inertia and accelerate nodes explicitly comes with the added benefit of true dynamic and is made possible by modern computers even for large systems cf. (Zhang and Chen 2014). The availability of computational power is of the utmost importance when choosing complexity of interactions and the computers of today favors better descriptions, e.g. beams over springs since reading from memory takes more time than computing. There is also the added benefit of the possibility of solution stability with a larger time step. The benefits of including angular interactions and its effect on poissons ratio is extensively examined by cf. Ostoja-Starzewski et al. (1996). Each part of the theoretical assumptions used in the model in this paper is thus not novel by them self, but combined in the currently most favorable combination for computational purposes.

The strategy used in this study is based on a mechanical particle interaction model and utilize known physical interactions and explicit solver/integration in time. The model's ability to capture real material behavior is first examined by comparing numerical results to experimental results found in literature. Then investigations are made on the microstructure's particle discretization: the role of the discrete particles' initial positions and the impact of any perturbations on the macroscopic global behavior.

2 The model

The model is based on a particle representation of the material. The movement of the particles governs the material behavior, and each particle holds a portion of the mass and moment of inertia of the material volume it represents, as illustrated in Fig. 1 for a grid representing a continuum. For the case when an element represents a separate physical entity such as a cell wall, the two particles representing it share mass and moment of inertia equally. The forces acting on each particle due to connections to surrounding particles are computed using algorithms picked from well-established geomet-
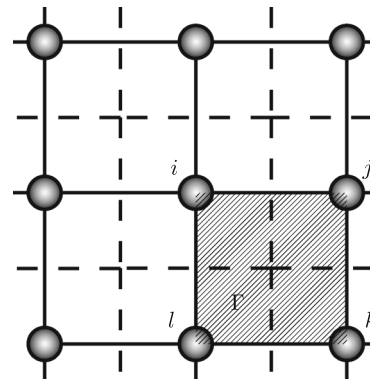
Fig. 1 Each particle holds mass m and moment of inertia I of the material volume element it represents. The interaction between particles are indicated by *solid lines* while the *dashed lines* indicates the small portion of volume each particle represent. Hence, material volumes may be shared (but not overlapped) by several particles such as in the case of the shaded volume Γ that is shared by particles i, j, k and l
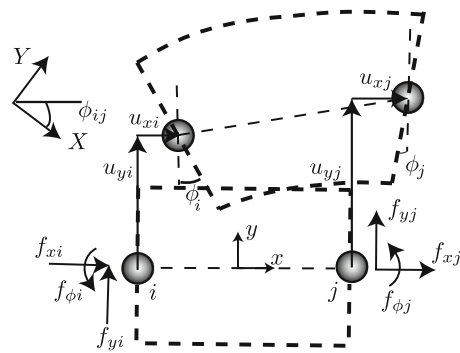
Fig. 2 A connection between the two particles i and j

rically nonlinear engineering beam theories (cf. Reissner 1972 or Krenk 2009) capable of capturing large rotations and deformations and fairly low length-to-width ratios of represented regions. Thus, each particle interacts with its neighbors and when the material deforms, each particle may be displaced and rotated. The present rotations of particle i and j are represented by ϕ_i and ϕ_j, respectively. This model does not utilize a stiffness matrix nor the cumbersome contact search and is thus computationally efficient. With reference to Fig. 2, in a local Cartesian coordinate system (x, y), with its x-axis oriented along the line connecting the particle i:s and j:s initial positions, the initial distance between the two particles is given by l_{ij} while the hori-

zontal and vertical displacements of particle i are given by u_{xi} and u_{yi}. It is assumed that the potential energy Φ_{ij} in the connection between particles i and j is given by:

$$\Phi_{ij} = \frac{1}{2} \int_0^{l_{ij}} EA_{ij}\epsilon_{ij}^2 + GA_{ij}\zeta_{ij}^2 + EI_{ij}\kappa_{ij}^2 dx, \quad (1)$$

where $\epsilon_{ij} = (1+\chi_{ij})\theta_2 + \eta_{ij}\theta_1 - 1$ is the current axial strain, $\zeta_{ij} = \eta_{ij}\theta_2 - (1+\chi_{ij})\theta_1$ is the current shear strain, $\kappa_{ij} = (\phi_j - \phi_i)/l_{ij}$ is the current bending strain (here, $\theta_1 = \sin(\phi_i/2 + \phi_j/2)$, $\theta_2 = \cos(\phi_i/2 + \phi_j/2)$, $\chi_{ij} = (u_{xj} - u_{xi})/l_{ij}$ and $\eta_{ij} = (u_{yj} - u_{yi})/l_{ij}$), cf. Persson and Isaksson (2014). The Young's modulus is given by E and the shear modulus by G, while the connection between particle i and j has width h_{ij}, height b_{ij}, cross section area $A_{ij} = b_{ij}h_{ij}$ and area moment of inertia $I_{ij} = b_{ij}h_{ij}^3/12$. The forces acting in the local coordinate system on each particle i due to the connection to particle j is obtained using their associated conjugate variables (i.e. displacements) according to $f_{xi} = \partial\Phi_{ij}/\partial u_{xi}$, $f_{yi} = \partial\Phi_{ij}/\partial u_{yi}$ and $f_{\phi i} = \partial\Phi_{ij}/\partial u_{\phi i}$. Using (1), the axial forces f_{xi} and f_{xj}, the transverse forces f_{yi} and f_{yj}, and the bending moments $f_{\phi i}$ and $f_{\phi j}$ are in the local coordinate system (x, y) readily given by (Fig. 2):

$$\begin{aligned}
f_{xi} = -f_{xj} &= EA_{ij}\theta_2\left[1 - \theta_2(\chi_{ij}+1) - \theta_1\eta_{ij}\right] \\
&\quad + GA_{ij}\theta_1\left[\theta_2\eta_{ij} - \theta_1(\chi_{ij}+1)\right] \\
f_{yi} = -f_{yj} &= EA_{ij}\theta_1\left[1 + \theta_2(\chi_{ij}+1) - \theta_1\eta_{ij}\right] \\
&\quad - GA_{ij}\theta_2\left[\theta_2\eta_{ij} - \theta_1(\chi_{ij}+1)\right] \\
f_{\phi i} &= EA_{ij}l_{ij}\left[\theta_2(\chi_{ij}+1) + \theta_1\eta_{ij} - 1\right]\left[\theta_2\eta_{ij}\right. \\
&\quad \left. - \theta_1(\chi_{ij}+1)\right]/2 \\
&\quad - GA_{ij}l_{ij}\left[\theta_2\eta_{ij} - \theta_1(\chi_{ij}+1)\right]\left[\theta_2(\chi_{ij}+1)\right. \\
&\quad \left. + \theta_1\eta_{ij}\right]/2 \\
&\quad - EI_{ij}\kappa_{ij} \\
f_{\phi j} &= f_{\phi i} + 2EI_{ij}\kappa_{ij} \quad (2)
\end{aligned}$$

For more details on the beam model the interested reader is directed to the work of Krenk (2009) or Persson and Isaksson (2013) for instructions concerning implementation. It is convenient to gather the forces due to the connection between particles i and j at time t in a vector according to ${}^t\bar{f}_{ij} = [f_{xi}, f_{yi}, f_{\phi i}, f_{xj}, f_{yj}, f_{\phi j}]^T$. For computational purposes, ${}^t\bar{f}_{ij}$, given in the connection's local coordinate system, is rotated to a fixed global Cartesian system (X, Y), Fig. 2, before the summation of all forces affect-

ing the particles are computed. This is achieved by using the well-known 2D rotation matrix ${}^t\bar{\bar{\Omega}}_{ij}$, with ϕ_{ij} being the angle between the local x-axis and the global X-axis:

$$\bar{\bar{\Omega}}_{ij} = \begin{bmatrix} \cos\phi_{ij} & -\sin\phi_{ij} & 0 & 0 & 0 & 0 \\ \sin\phi_{ij} & \cos\phi_{ij} & 0 & 0 & 0 & 0 \\ 0 & 0 & 1 & 0 & 0 & 0 \\ 0 & 0 & 0 & \cos\phi_{ij} & -\sin\phi_{ij} & 0 \\ 0 & 0 & 0 & \sin\phi_{ij} & \cos\phi_{ij} & 0 \\ 0 & 0 & 0 & 0 & 0 & 1 \end{bmatrix}$$

(3)

Using (3), the relations between forces and displacements in global and local systems are

$${}^t\bar{F}_{ij} = {}^t\bar{\bar{\Omega}}_{ij}^{-1}\,{}^t\bar{f}_{ij} \quad \text{and} \quad {}^t\bar{u}_{ij} = {}^t\bar{\bar{\Omega}}_{ij}\,{}^t\bar{U}_{ij}, \quad (4)$$

where ${}^t\bar{U}_{ij}$ is the vector containing particle i:s and j:s displacements in the global coordinate system at time t (${}^t\bar{U}_{ij} = \left[U_{xi}, U_{yi}, \phi_i, U_{xj}, U_{yj}, \phi_j\right]^T$), note that $\phi_i = U_{\phi i}$ as a result of the element formulation (Fig. 2). Hence, the forces on the two particles due to their interaction only, is given in the vector ${}^t\bar{F}_{ij}$ in the global coordinate system at time t. All forces and moments acting on a specific particle i at time t, according to (4), are summed up, in the global frame of reference, to a force vector ${}^t\bar{F}_i$. It is noticed that each particle may interact with an arbitrary number of particles, depending on the geometry and how the connections of the particles are defined, i.e. a grid. A semi-implicit Euler method (cf. Cromer 1981) governs the advancement in time, i.e.

$$\begin{aligned}
{}^{t+\Delta t}\ddot{\bar{U}}_i &= \bar{\bar{M}}_i^{-1}\,{}^t\bar{F}_i \\
{}^{t+\Delta t}\dot{\bar{U}}_i &= (1-\lambda)\,{}^t\dot{\bar{U}}_i + {}^{t+\Delta t}\ddot{\bar{U}}_i\Delta t \\
{}^{t+\Delta t}\bar{U}_i &= {}^t\bar{U}_i + {}^{t+\Delta t}\dot{\bar{U}}_i\Delta t
\end{aligned}$$

(5)

where Δt is a small time-step increment, a dot $\dot{()}$ denote a time derivative of the variable, λ a damping coefficient simulating internal friction and $\bar{\bar{M}}_i$ is a mass matrix given by

$$\bar{\bar{M}}_i = \begin{bmatrix} m_i & 0 & 0 \\ 0 & m_i & 0 \\ 0 & 0 & \alpha m_i \end{bmatrix}$$

(6)

In (6), $m_i = \frac{1}{2} \sum_j A_{ij} l_{ij} \rho_{ij}$ is the mass of particle i, which is connected to particle j with element crosssectional area A_{ij}, initial length l_{ij} and density ρ_{ij}. The arbitrary constant α is chosen to represent the angular moment of inertia and is supposed to be small. For this model, $\alpha = 1/1000$ has proved to yield good results. Then, when the global displacements of all particles have been updated, they are rotated back to the global systems according to (4). Needless to say, at every time step t, particle i:s position in the global coordinate system is given by the position vector ${}^t \bar{R}_i$

$$ {}^t \bar{R}_i = {}^{t=0} \bar{R}_i + {}^t \bar{U}_i. \tag{7} $$

Finally, when the strain energy density in the connection segment between particles i and j exceeds a specific critical strain energy density Ψ_0, the connection fractures instantly whereupon the interaction between the two involved particles is immediately canceled. The strain energy density ${}^t \Psi_{ij}$ at time t is calculated at the position initially located exactly in-between the two particles i and j, using (1), and is a function of the present deformations according to

$$ {}^t \Psi_{ij} = \frac{E}{2} [1 - \theta_2 (\chi_{ij} + 1) - \theta_1 \eta_{ij}]^2 $$
$$ + \frac{G}{2} [\theta_2 \eta_{ij} - \theta_1 (\chi_{ij} + 1)]^2 + \frac{E I_{ij}}{2 A_{ij}} \kappa_{ij}^2 \tag{8} $$

When deriving (8) it is assumed that the strain energy density is constant in the volume element. This is a fair physical approximation for sufficiently small volume elements. Cracks may nucleate, propagate or coalesce at any time at arbitrary connection segments if the local fracture criterion is fulfilled during the simulation. Hence, there is no need for any predefined crack path or crack growth criterion. For more details concerning the model, the interested reader is directed to Persson and Isaksson (2013; 2014).

3 Comparisons to experiments

Two different geometries are used for numerical comparisons to experiments found in literature. In both examples it is assumed that linear elasticity prevails and that the material can be considered isotropic.

3.1 Geometries

The first test geometry is picked from Fred Nilsson's pioneering work (Nilsson 1974). A strip specimen,
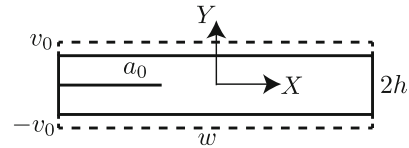
Fig. 3 Illustration of a strip specimen with clamped edge displacement of $\pm v_0$

illustrated in Fig. 3, of width $w = 30.5$ cm, height $2h = 23$ cm and thickness $B = 0.1$ mm, has a stationary initial edge crack with length a_0. A state of plane stress prevails. The material has the Young's modulus $E = 196$ GPa, the Poisson's ratio $\nu = 0.3$, the shear modulus $G = \frac{E}{2(1+\nu)} = 75.4$ GPa, a density $\rho = 7900$ kg/m^3, a fracture toughness $K_c = 106$ MN/m$^{3/2}$ and shear wave speed

$$ c_2 = [G/\rho]^{1/2} = 3100 \text{ m/s.} \tag{9} $$

The top and bottom horizontal edges are slowly displaced in opposite directions, as illustrated in Fig. 3, so that the existing crack opens. The classical criterion for crack growth initiation is applied, i.e. crack growth is assumed to initiate when the opening mode stress intensity factor $K_I \geq K_c$. For the loading situation considered here (cf. Nilsson 1974), this means that when the magnitude of the displacements v_0 reaches $v_0 = v_c = h K_c (1 - \nu^2) / [E \sqrt{\pi a_0}]$ the crack starts to propagate. This is in the model accomplished by setting the local fracture energy density Ψ_0 equal to the highest present energy density in the body. The global energy density required to drive the crack is given by the fracture surface energy density γ_f,

$$ \gamma_f = v_c^2 E / [2h(1 - \nu^2)], \tag{10} $$

and is uniquely related to both the stress intensity factor K_I and the propagation velocity (Nilsson 1974). When the crack is released, it initially grows with a fluctuating velocity v which soon reaches a plateau, or steady state, that holds until the crack tip approaches the opposite vertical boundary.

The second test geometry is an impulse loaded threepoint bending test (cf. Zehnder and Rosakis 1990). A hammer with mass $m_h = 195$ kg and velocity v_h is dropped on the center of a steel cantilever with an impact velocity of $h_h = v_I = -5.0$ m/s at time $t=0$,
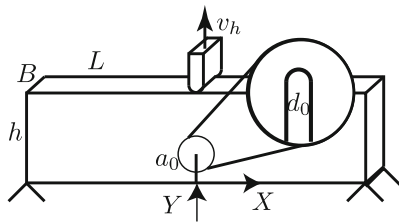
Fig. 4 Illustration of a three-point impulse loaded bending test of a cantilever. The radius of the crack tip is given by $d_0/2$
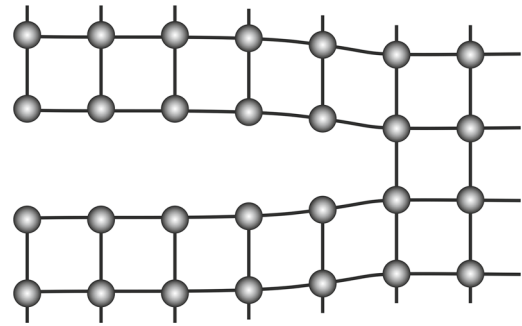

Fig. 5 A small part of a regular square grid with an *opened crack*

illustrated in Fig. 4. The cantilever has length $L = 30.4$ cm, height $h = 12.8$ cm, thickness $B = 0.95$ cm, density $\rho = 7900$ kg/m^3, Young's modulus $E = 196$ GPa, a fracture toughness $K_c = 62$ MPa$\sqrt{\text{m}}$ and an edge crack of length $a_0 = 0.29h$ positioned at the center of the cantilever. The fracture toughness needs to be translated to a critical strain energy density for the model. This could of course be done analytically, but for simplicity it is done in a separate simulation where the cantilever is loaded with a force F, applied at the center of the beam, such that the stress intensity factor $K_I = K_c$, i.e.

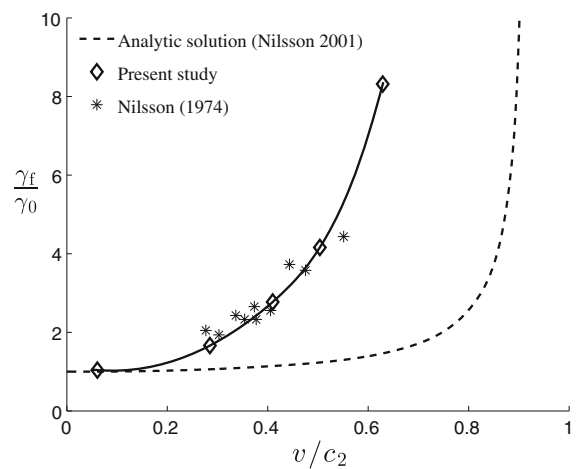$$K_I = \frac{FL}{Bh^{\frac{3}{2}}} f(a_0/h), \tag{11}$$

where $f(a_0/h) = 1.5$ (cf. Nilsson 2001). The resulting strain energy density at the crack tip is utilized as the fracture energy density Ψ_0 in the following dynamic simulations.

3.2 Results

Both experimental geometries are here discretized by regular rectangular square grids having equal spacings in vertical and horizontal directions. In the first example, which simulates the experiments by Nilsson (1974), the specimens are represented by grids consisting of 200 particles in the horizontal direction and 75 particles in the vertical direction, giving an initial separation length between particles of $l_0 = w/199$ (the particles are positioned at the grid intersections). A small part of a grid, with the crack slightly opened, is illustrated in Fig. 5. The time-integration parameters are set to $\Delta t = 0.01$ ns and $\lambda = 3 \cdot 10^{-6}$. The simulated results are shown in Fig. 6 with a_0 varied in the interval $1 \leq a_0/l_0 \leq 10$. The high steady-state velocities are
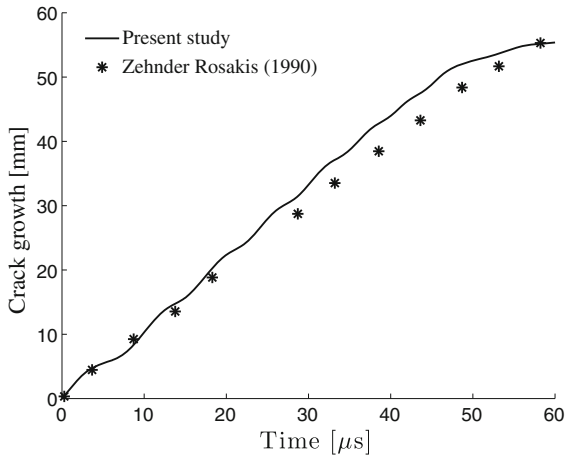

Fig. 6 Comparison of the simulated results, using regular square grid cells, with the experimental results of Nilsson (1974). *Stars* represent the experimental results and *diamonds* the results of the simulations. The results are contrasted with an analytical solution (*dashed line*) given by Nilsson (2001). The quasi-static fracture surface energy density is given by γ_0

obtained for low initial crack lengths a_0. The quasi-static solution gives $\gamma_0 = v_0^2 \pi a_0 E / [2h^2(1 - v^2)^2]$. Nilsson also presented an analytical solution to the problem of the crack in an infinite strip (Nilsson 2001). This solution neglect energy dissipation in the material, and thus over-estimates the crack propagation speed, and it is included as a reference with that in mind. Notice that there is a considerable difference between the simplified analytical solution and the experimental results as well as the numerical results, both in the magnitude of the speed and the shape of the curve, which will be further discussed later on.

Fig. 7 Comparison of the simulated results, using regular rectangular grids, with the experimental results of Zehnder and Rosakis (1990). Crack growth versus time in the impulse loaded three-point bending model

In the second example, which simulates the experiments by Zehnder and Rosakis (1990), the crack tip has a finite radius of $d_0/2 = 0.7$ cm. In the simulations, the distance d_0 is set as the spacing of the regular grid meaning that a grid consist of 218 by 92 particles in horizontal and vertical directions, respectively. The two lower supporting corners are held fixed in the vertical direction during the simulation while 10 particles in contact with the hammer moves along with the hammer, i.e. $\bar{U}_i = \left[0, \int_0^t v_h t dt, 0\right]_i^T$ for particle i which is one of the 10 particles in contact with the hammer. The reaction force from the particles slows down the hammer according to $v_h = v_I + \int_0^t F_r/m_h dt$, where $F_r = \sum_i F_i^r$ and F_i^r is the vertical component (Y-direction) of the reactive force vector of particle i, which is in contact with the hammer. The integration parameters are $\Delta t = 0.01$ ns and $\lambda = 10^{-7}$. The resulting crack growth is shown in Fig. 7.

3.3 Discussion of the experimental comparisons

In the two compared examples, i.e the results in Figs. 6 and 7, it is shown that the model captures the dynamic fractures remarkably well. In the first example, the strip, the cracks advances as the external boundaries are held stationary when the crack growth has initiated, while in the second example, the impulse loaded beam, the crack propagates when the external boundaries

moves, which demonstrates the diversity of the model. In Fig. 6 there is a considerable difference between the experimental data and the analytical model. There are a few plausible explanations for this, but energy dissipation is most likely the main reason. In the region of the experimental data the numerical model agrees well with the experiments, and outside this region the behavior agrees phenomenological with the analytical model, however with a shift in the maximum crack propagation speed. Nilsson (1972) speculate that plasticity processes in the crack tip region might have an important role in the crack propagation in this case. This might agree with our results since fairly large amounts of energy dissipation takes place in the model. The first data point in Fig. 6 is special in the sense that it does not represent a continuous growth but a series of interrupted cracks. It should thus not to be seen as having a lower crack speed than the limiting $0.28c_2$ established by Marder and Liu (1993).

The modeling of the beam impacted by a drop hammer, i.e. the ballistic experiment of Zehnder and Rosakis (1990), also agree well with the experiments. However, the simulation shows some oscillations in the crack speed that the experimental resolution is to course to capture. At the instances when the crack grows, it grows at a constant speed of $0.5c_2$. Between the times of growth are moments of crack arrest, and together this results in an average crack propagation of $0.3c_2$ on the global scale which corresponds well to the reported experimental one, Fig. 7. Both this crack growth speed of $0.5c_2$, and the slowing effect of the oscillations agrees with the work with double cantilever beam by Kanninen (1974). With a shear wave speed c_2 of roughly 3100 m/s, the 3μs of the first diversion from the initial crack speed corresponds to the time a shock-wave, originating at the first crack growth event, need to reach the closest free edge, reflect and meet the moving crack. This interference phenomenon seems to have a great influence and somewhat slows down the crack growth velocity.
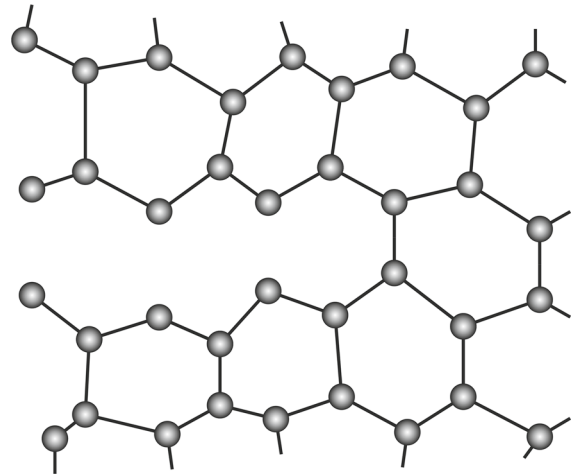
4 Material discretization

4.1 Cellular microstructure

To investigate a material with cellular (or porous) microstructure, a honeycomb grid is used to simulate the materials in the experiments by Nilsson (1974),
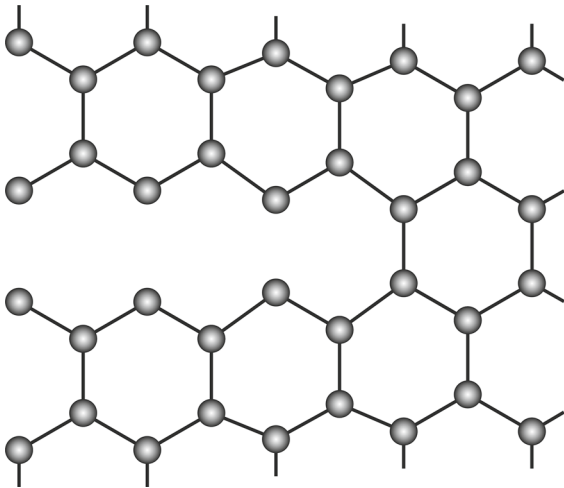
Fig. 8 Illustration of a part of a regular honeycomb structure with an *opened crack*. Each cell wall have length l_0


Fig. 11 Illustration of a part of a perturbed honeycomb grid with an *opened crack*
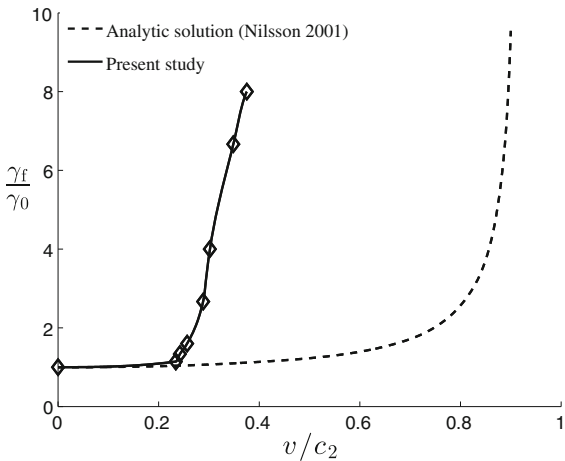

Fig. 9 Crack surface energy density versus steady-state velocity for regular honeycomb grids, the diamonds are the computed values and the *dashed line* is the analytical solution to the continuous infinite strip cf. Nilsson (2001)

instead of the previously used rectangular grids. The honeycomb structures are built of regular hexagons as illustrated in Fig. 8. The cell walls have length $l_0 = w/50$ and thickness $l_0/10$, resulting in 46 by 35 cells and an effective density of 0.12ρ. Note that this discretization represent an ideal honeycomb material, it is not another discretization of the same continuous specimen as above because the microstructure has now regularly spaced open cells. The particles are positioned at each end of each cell wall and the cell walls are made of the same material as in the example above. The time integration parameters are $\Delta t = 0.01$ ns and $\lambda = 3 \cdot 10^{-6}$. The result is shown in Fig. 9, with $5 \le a_0/l_0 \le 50$, i.e. 3 to 30 prefractured cells out of 46. The graph shows the fracture surface energy as a function of the crack propagation velocity. Note that although the effective density of the structure is less than the density of the material, and the proper shear wave speed might be different in a honeycomb structure than in a continuous material, the shear wave speed c_2,

Fig. 10 Illustration of a part of a perturbed square grid with an opened crack (*left*). Illustration of a perturbed square (*right*)
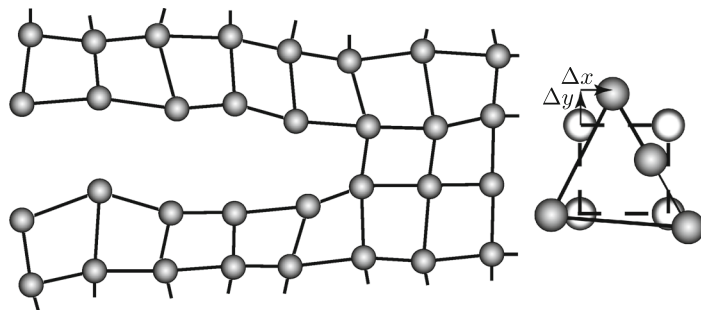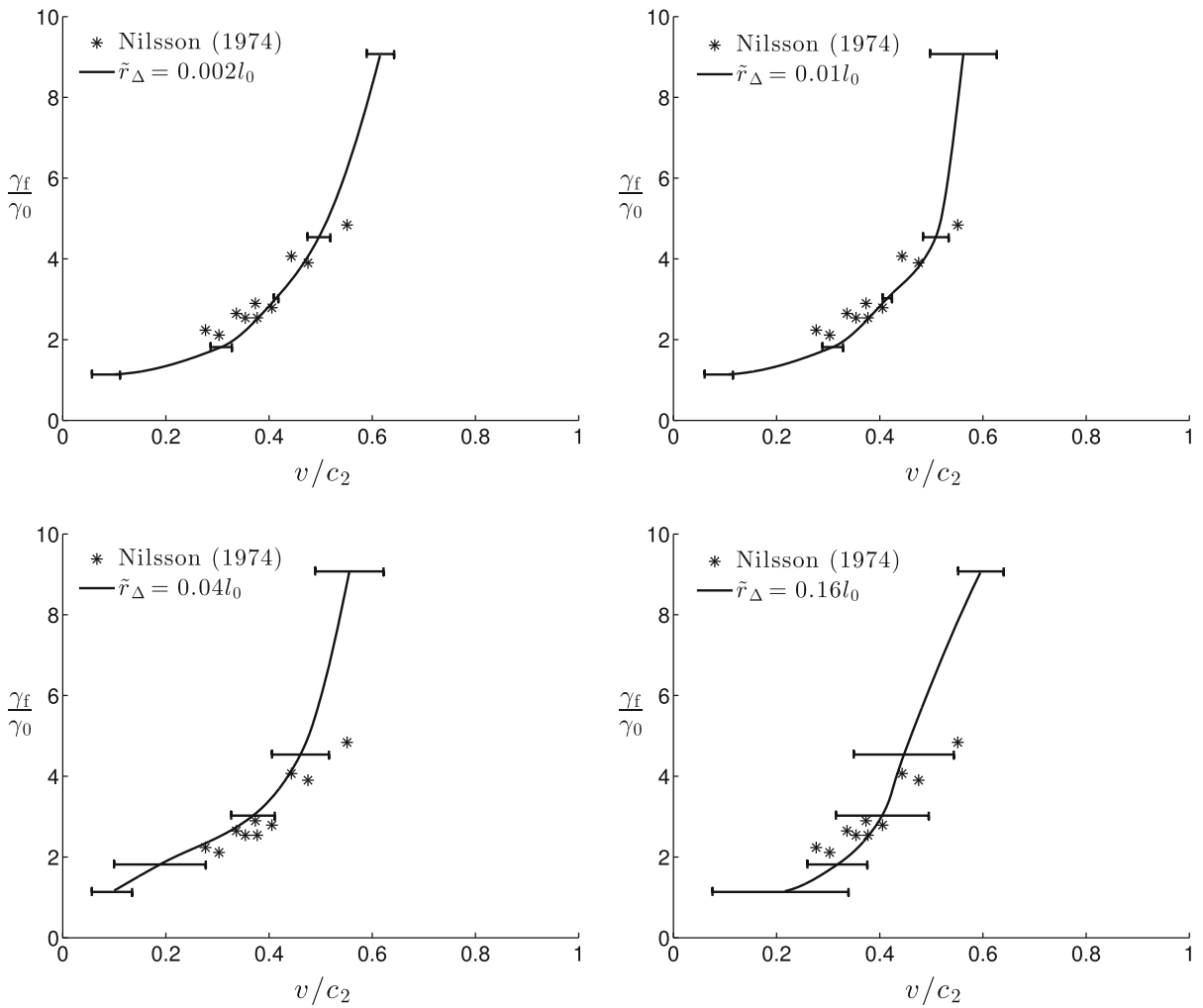
Fig. 12 Fracture propagation energy versus steady-state velocity for perturbed rectangular grids. The *solid line* represents the average values and the *bars* are the standard deviation. *Stars* are the experimental results of Nilsson (1974)

as well as the crack propagation energy density γ_f, is calculated for the bulk material in accordance to (9) and (10). This example is included because the numerical results are interesting.

4.2 Results and discussion

The numerical crack propagation speed versus fracture surface energy is displayed in Fig. 9. The analytic solution for the undamped continuum of Nilsson (2001) is included as a reference. There is a phenomenological similarity between the analytic solution and the numerical results in that there is a significant increase in crack surface energy once certain crack speed is reached.

Although there is a considerable difference in when this shift occurs, once the shift is reached the increase in fracture surface energy is similar.

5 Perturbation of the particles' initial positions

5.1 Irregular grid configuration

So far, the material has been discretized by regular grids. However, any real world material is likely to differ from a perfect regular grid. For the purpose of capturing the mechanical fracture behavior of imperfect material microstructures, the grids used in previous sections are slightly perturbed. A perturbation

is in this case a random shift of the grid-nodes, i.e. a shift of the particles' initial positions. Figures 10 and 11 shows parts of perturbed grids with opened cracks.

The regular rectangular grid of the strip specimen in Sect. 3.1 is subjected to a random perturbation, Δx and Δy (different at all grid-nodes), as illustrated in Fig. 10. The magnitude of the perturbation $r_\Delta = [\Delta x^2 + \Delta y^2]^{1/2}$ is small enough to ensure the connection order of the particles is kept and that the material is still isotropic on the global scale. For the different grids the average perturbation $\tilde{r}_\Delta$ varies in the interval $0.002 \leq \tilde{r}_\Delta / l_0 \leq 0.16$, where l_0 is the constant distance between initial particle positions in the undisturbed grid. The time integration parameters are $\Delta t = 0.01$ ns and $\lambda = 3 \cdot 10^{-6}$. The computed fracture surface energies in terms of the average and standard deviations from 10 different grids for each level of perturbation, are shown in Fig. 12. The initial crack length varied in the interval $1 \leq a_0 / l_0 \leq 10$. Similarly, the honeycomb geometry in Sect. 4 is randomly perturbed, as illustrated in Fig. 11. Also here, the perturbation is limited so the connection order of the particles is kept. Twenty different structures, for each level of fracture surface energy, all having $\tilde{r}_\Delta / l_0 = 0.16$ are simulated and the result is presented in Fig. 13, with time integration parameters $\Delta t = 0.01$ ns and $\lambda = 3 \cdot 10^{-6}$. The initial crack length varied between 3 and 30 cells.

5.2 Results and discussion

The computed crack growth velocity versus fracture surface energy for the perturbed grids are displayed in Figs. 12 and 13. The result in Fig. 12 demonstrates that even a small perturbation of initially ordered regular grids (continuous microstructure) may change the crack growth behavior, and with $\tilde{r}_\Delta / l_0 = 0.04$ the scatter in the results closely match the scattering in the experimental data. With $\tilde{r}_\Delta / l_0 = 0.16$ the scatter in the numerical model greatly exceeds those of the experiments in Nilsson (1974). However, even with the highest level of perturbation, there is no change in the shape of the curve and there is no categorical shift in the relation between crack speed and crack surface energy.

When comparing the perturbed honeycomb (discontinuous microstructure) in Fig. 13 with the unperturbed in Fig. 9 there is a slight shift towards higher crack growth speeds. A possible explanation is that energy
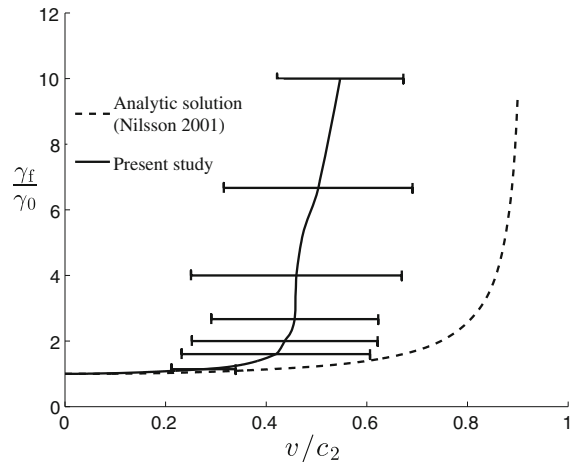
Fig. 13 Fracture propagation energy versus steady-state velocity for irregular honeycomb grids. The *solid line* represents the average values and the *bars* are the standard deviation. The *dashed line* is the analytical solution cf. Nilsson (2001)

travels the shortest/fastest path in the material. A perturbed honeycomb cell may be both stiffer and less stiff than the regular geometry, and even though the average path may be slower, the fastest path may be faster in the perturbed honeycomb. This phenomenon is very small in the rectangular grids representing continuous microstructures and is not observable.

6 Conclusions

In the examples in Sect. 3.1 it has been shown that the model captures dynamic fracture both driven by elastic energy with stationary boundaries and cracks driven by energy supplied by moving boundaries, which demonstrates the diversity of the model. The comparison to the impact experiment is of particular interest since the numerical model have a higher resolution of the crack growth behavior and is on a length scale that is below the detection limit of most instruments, and which is essential to the crack growth. The model has been used to illustrate difference in crack growth behavior in materials having fairly continuous and discontinuous (cellular) microstructures. The influence of perturbations in a discontinuous microstructure is significantly larger than the influence of perturbations in continuous microstructures. A perturbed regular grid, i.e. a fairly continuous microstructure, might be interpreted as a grained material microstructure, and may explain the scatter in the experimental data observed in Nilsson

([1974](#)). It is interesting to note that although all fracture in this study has been of a truly brittle manner, it captures the fracture behavior of more ductile materials such as a steel plate. This support the hypothesis that heat and sound (vibrations) are important parts of the energy dissipation in dynamic fracture and may be of a greater importance than the energy lost due to plastic deformation. Finally, capturing a discontinuous microstructure well is very important when analyzing growing cracks in cellular materials such as solid foams or wood, and the accuracy of the predictions on solid foam fracture, which for most foams have a ductile component will be investigated in a forthcoming study.

References

Bathe KJ (2006) Finite element procedures. Prentice-Hall, Pearson education Inc, New Jersy

Belytschko T, Gracie R, Ventura G (2009) A review of extended/generalized finite element method for material modeling. Model Simul Mater Sci Eng 17:043001

Bolander JE, Saito S (1998) Fracture analysis using spring networks with random geometry. Eng Fract Mech 61:569–591

Cromer A (1981) Stable solutions using the Euler approximation. Am J Phys 49:455–459

Fahrenthold EP, Horban AB (2001) An improved hybrid particle-element method for hypervelocity impact simulation. Int J Impact Eng 26:169–178

Freund LB (1998) Dynamic fracture mechanics. Cambridge University Press, Cambridge

Gao H (1996) A theory of local limiting speed in dynamic fracture. J Mech Phys Solids 44:1453–1474

Gehlen PC, Popelar CH, Kanninen I (1987) Modeling of dynamic crack propagation: I. validation for one-dimensional analysis. Int J Fract 15:281–294

Gerstle W, Sau N, Silling S (2007) Peridynamic modeling of concrete structures. Nucl Eng Des 237:1250–1258

Griffith AA (1920) The phenomena of rupture and flow in solids. Philos Trans R Soc Lond A 221:163–198

Ha YD, Bobaru F (2010) Studies of dynamic crack propagation and crack branching with peridynamics. Int J Fract 162:229–244

Hrennikoff A (1941) Solution of problems of elasticity by the framework method. J Appl Mech 8(4):A169–A175

Kanninen MF (1974) A dynamic analysis of unstable crack propagation and arrest in the DCB test specimen. Int J Fract 10:415–430

Krenk S (2009) Non-linear modeling and analysis of solids and structures. Cambridge University Press, Cambridge

Marder M, Liu X (1993) Instability in lattice fracture. Phys Rev Lett 71:2417–2420

Monteiro Azevedo N, Lemos JV (2006) Hybrid discrete element/finite element method for fracture analysis. Appl Mech Eng 195:4579–4593

Mos N, Dolbow J, Belytschko T (1999) A finite element method for crack growth without remeshing. Int J Numer Method Eng 46:131–150

Nilsson F (2001) Fracture mechanics—form theory to applications. Fingraf, Södertälje

Nilsson F (1974) Crack propagation experiments on strip specimens. Eng Fract Mech 6:397–403

Ooi ET, Yang ZJ (2011) Modelling dynamic crack propagation using the scaled boundary finite element method. Int J Numer Methods Eng 88:329–349

Ostoja-Starzewski M, Sheng PY, Alzebdeh K (1996) Spring Network models in elasticity and fracture of composites and polycrystals. Comput Mater Sci 7:82–93

Persson J, Isaksson P (2013) A particlebased method for mechanical analyses of planar fiber-based materials. Int J Numer Methods Eng 93:1216–1234

Persson J, Isaksson P (2014) A mechanical model for rapid deformation and fracture in 3D fiber materials with ability to handle length effects. Int J Solids Struct 51:2244–2251

Popelar CH, Gehlen PC (1987) Modeling of dynamic crack propagation: II. Validation of two-dimensional analysis. Int J Fract 15:159–177

Rabb RJ, Fahrenthold EP (2010) Impact dynamics simulation for multilayer fabrics. Int J Numer Methods Eng 83:537–557

Ramulu M, Kobayashi AS (1985) Mechanics of crack curving and branshing—a dynamic fracture analysis. Int J Fract 27:187–201

Reissner E (1972) On one-dimensional finite-strain beam theory: the plane problem. J Appl Math Phys 32:795–804

Silling SA, Bobaru F (2005) Peridynamic modeling of membranes and fibers. Int J Non-Linear mech 40:395–409

Silling SA, Askari E (2005) A meshfree method based on the peridynamics model of solid mechanics. Comput Struct 83:1526–1535

Suiker ASJ, Metrikine AV, de Borst R (2001) Comparison of wave propagation characteristics of the Cosserat continuum model and corresponding discrete lattice models. Int J Solids Struct 28:1563–1583

Wang G, Al-Ostaz A, Cheng AH-D, Mantena PR (2009) Hybrid lattice particle modeling: theoretical considerations for a 2D elastic spring network for dynamic fractrue simulations. Comput Mater Sci 44:1126–1134

Zang W, Gudmundson P (1988) A boundary intergral method for internal piece-wise smooth crack problems. Int J Fract 38:275–294

Zehnder AT, Rosakis AJ (1990) Dynamic fracture initiation and propagation in 4340 steel under impact loading. Int J Fract 43:271–285

Zhang Z, Chen Y (2014) Modeling nonlinear slastic solid with correlated lattice bond cell for dynamic fracture simulation. Compu Methods Appl Mech Eng 279:325–347